Chemistry Europe
European Chemical Societies Publishing
Batteries & Supercaps

RESEARCH ARTICLE OPEN ACCESS

Pressure-Induced Degradation Effects in Large-Format Lithium-Ion Pouch Cells

Tobias Hölderle[1,2] | Anna Smith[3] | Nils Schmidgruber[4] | Volodymyr Baran[5] | Alexander Schökel[5] | Lea Westphal[1,2] | Vladislav Kochetov[2] | Steffen Jokisch[3] | Peter Müller-Buschbaum[1] | Anatoliy Senyshyn[1,2]

[1]Department of Physics, Chair for Functional Materials, TUM School of Natural Science, Technical University of Munich, Garching, Germany | [2]Heinz Maier-Leibnitz Zentrum (MLZ), Technical University of Munich, Garching, Germany | [3]Institute for Applied Materials (IAM), Karlsruher Institute of Technology (KIT), Eggenstein-Leopoldshafen, Germany | [4]Wbk Institute of Production Science, Karlsruher Institute of Technology (KIT), Karlsruhe, Germany | [5]Deutsches Elektronen-Synchrotron DESY, Hamburg, Germany

Correspondence: Anatoliy Senyshyn (anatoliy.senyshyn@frm2.tum.de; anatoliy.senyshyn@gmail.com)

Received: 5 December 2025 | **Revised:** 22 February 2026 | **Accepted:** 9 March 2026

Keywords: electrochemical aging | inhomogeneous lithiation | large-format lithium-ion pouch cells | pressure-induced degradation | thermal management | X-ray radiography

ABSTRACT

The electrochemical aging of large-format pouch cells (LG E78 type) is systematically studied under varying external pressure. The cells are cycled at high current while combining reference performance testing, direct current internal resistance measurements, and temperature monitoring to track the degradation. Further synchrotron-based powder X-ray diffraction radiography measurements of the cells are carried out in a fresh and aged state, resolving the spatial lithium concentration in the graphite anodes and NMC cathodes. Cycling under external pressure strongly influences cycling stability, resistance evolution, and thermal behavior. Without pressure, the tested cell shows the highest initial depth-of-discharge (DOD) but rapid capacity fade, accelerated resistance growth, and elevated temperatures. Under pressure, the cells exhibit longer lifetimes and improved heat dissipation but also show pressure-induced ionic transport limitations and pronounced lithiation inhomogeneities, including a ring-like lithium distribution linked to electrolyte redistribution and pore size reduction. It is shown that reduced pressure emerged as the most favorable compromise, balancing structural stability, lithium homogeneity, and cycle life.

1 | Introduction

The rapid transition toward carbon neutrality and electrification of transportation brought lithium-ion batteries (LIBs) to the center of the global energy strategies. Since the commercialization of LIBs by Sony in 1991, demand has increased rapidly, evolving from applications in small consumer electronics to the dominant technology in large-scale storage units for electric vehicles (EVs) and stationary energy storage [1, 2]. This success builds directly on their capability to deliver high energy density, long cycle life, and efficiency, achieved by the use of nickel-rich layered oxide cathodes and advanced graphite-based anodes, which form the backbone of today's commercial large-format cells [3–5]. Such achievement is based on laboratory-scale research, which provided fundamental insights into LIB behavior. Small-format cells, such as coin cells, three-electrode cells, and miniature pouch cells, are commonly used to evaluate electrode materials, interfacial phenomena, and degradation mechanisms [6–12]. These studies have provided valuable information on reaction kinetics, structural evolution, safety, and the occurrence of aging mechanisms, including lithium plating and electrode inhomogeneity [13–15]. Furthermore, experimental diffraction-based techniques are crucial in resolving the degradation of LIBs by focusing on the structural evolution of electrodes at the atomic level [16–21]. While such systems provide critical material-level insights, they often benefit from experimental advantages, which do not always translate to larger, commercially relevant cells. Thus, the scale-up from lab cells to large commercial cells, such

as 4680 cylindrical cells or high-capacity automotive prismatic and pouch cells, introduces numerous experimental and methodological challenges. Large-format cells display distinct electrochemical and mechanical characteristics due to their complex internal architectures [22–25], resulting in increased heterogeneous current distribution [26–28], nonuniform lithiation [29], internal mechanical stress [30], and differential heat generation [31], which are less pronounced in small-scale studies. However, cylindrical and prismatic cells often benefit from robust mechanical casings that provide consistent internal pressure and improved structural integrity. Pouch cells, in contrast, are more flexible and lightweight, allowing for higher gravimetric energy densities, which makes them attractive for automotive applications, where high energy density per unit weight and adaptable module design are key requirements [32]. Their performance, however, strongly depends on external mechanical stabilization, making stack pressure a central parameter in both design and operation. Previous studies have shown that mechanical pressure can improve the contact between electrodes and separators, prevent delamination, and enhance ionic conductivity, thereby contributing to improved cycle life and safety [33–37]. However, other reports have indicated a negative effect on the LIB performance at excessive stack pressure [38–41]. Taken together, these findings highlight that mechanical pressure has a nontrivial influence and requires careful optimization to balance performance, safety, and durability.

In this work, the pressure-dependent performance of large-format commercial pouch cells (LG Chem E78) is systematically studied. The E78 cell features an industrial-scale electrode design and multilayer pouch architecture, making it a representative model system for investigating mechanical effects under realistic operating conditions. The investigations focused on long-term cycling performance, lithium redistribution, and the evolution of electrochemical resistance and temperature, utilizing a comprehensive set of techniques that included electrochemical cycling, direct current internal resistance (DCIR) analysis, temperature monitoring, and synchrotron powder X-ray diffraction (PXRD) radiography. This combined approach enabled direct correlation of macroscopic cell behavior with electrode-level structural changes under defined mechanical constraints, thereby bridging the gap between laboratory-scale studies and industrial applications.

2 | Experimental Section

2.1 | Studied Cells

A series of commercially available LIBs of pouch cell format (LG Chem E78) was selected. The cells were like those reported previously in Refs. [24, 25, 42]. The chosen large-format cells (dimensions shown in Figure 1a -545 mm long edge, 98 mm width, and 9 mm thick, as reported in Ref. [21]) employ a nickel manganese cobalt oxide (NMC) cathode and a silicon-free graphite (Gr) anode chemistry [43]. In its fresh state, the cell displays a nominal voltage of 3.67 V, a capacity of 78 Ah (rated at 25°C with a 0.3°C charge current), and a delivered energy of 286 Wh. The corresponding minimum gravimetric and volumetric energy densities are 265 Wh/kg and 602 Wh/L, respectively [42]. The cells' interiors consist of a stacked electrode assembly comprising 20 double-sided anode sheets, 19 double-sided cathode sheets, and 40 separator sheets, all arranged in a layered manner. The stack is fixed with glue tapes and is enclosed in a laminated polymer pouch [25].

2.2 | Electrochemical Cycling

The studied large-format pouch cells required special handling and additional support during electrochemical cycling. All cycling procedures were performed at a controlled temperature of 25°C (±1°C) within the test field of the KIT Battery Technology Center (KIT-BATEC, Eggenstein-Leopoldshafen, Germany). A Basytec HPS cell tester system (capable of supplying currents up to 200 A and operating within a voltage range of 0–6 V) was used. The pouch cells were cycled within the full operational voltage window of 3.0–4.2 V. The cycling process consisted of a sequence of cycles, followed by a subsequent reference performance cycle (RPC) protocol, used to track the cell's state-of-health (SOH).

The cycling sequence consisted of 200 individual cycles, each consisting of a separate charge and discharge phase. The charging was carried out using a constant current–constant voltage

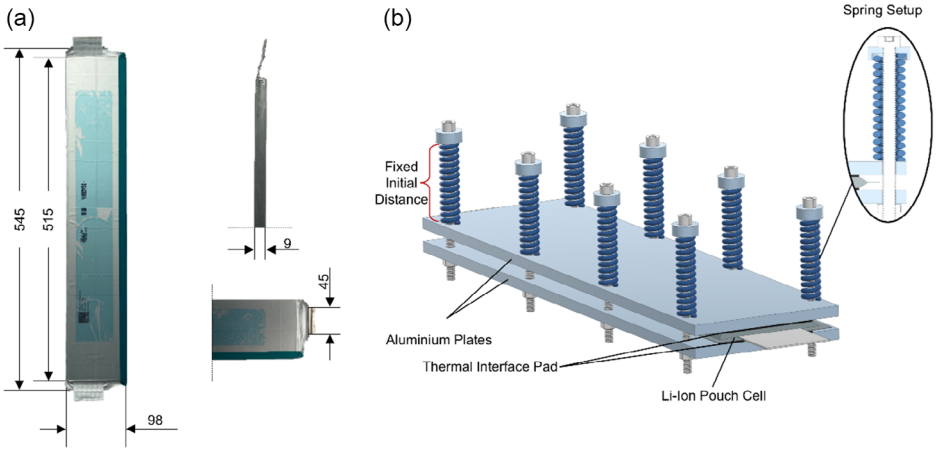

FIGURE 1 | Battery cell dimensions in mm for an exemplary E78 cell (a) and the detailed schematic of the high pressure setup (1.2 bar) realized by a spring-loaded mechanism acting on the top plate.

(CC–CV) protocol: a 1C constant current (78 A) charge until 4.2 V was reached, followed by a constant voltage phase at 4.2 V with a cutoff current of C/20 (3.9 A). The discharge phase was performed using a constant current of 2C (156 A) until the voltage reached 3.0 V. After the completion of 200 cycles (finished at the charged state), an additional RPC was performed to check the cell's SOH, which was used to determine if the electrochemical cycling should continue.

The RPC consisted of a series of characterizations: First, a slow discharge was applied using a constant current of C/10 (7.8 A) down to 3.0 V to fully discharge the cell. Following this, the reference charge cycle was initiated with a constant C/10 current until the voltage reached 4.2 V, followed by a constant voltage phase with C/20 limit. Subsequently, a constant discharge using C/10 was applied again until the cell reached 3.0 V (this capacity was used to measure the evolution of the SOH of the cells). A series of DCIR measurements were conducted at defined state-of-charge (SOC) levels of 10%, 30%, 50%, 70%, and 90%, which were adjusted using an Ah-counter and a subsequent relaxation time of 15 min. DCIR characterization was carried out by applying a pulse with a current of 1C (78 A) for 20 s, which allowed the determination of SOC-dependent internal resistances. After the final DCIR pulse, the cell was fully recharged in preparation for the next cycling sequence.

For cells adopting Gr|NMC chemistry, the end-of-life (EOL) criterion is typically defined around 70%–80% SOH [44, 45], corresponding to the transition from a linear degradation regime to an accelerated and nonlinear degradation mode, often referred to as the knee point [46]. In the current study, an SOH threshold of 80% was selected as the cutoff point for electrochemical cycling to ensure consistency with the given literature EOL standards. In total, three cells were cycled using this protocol, each under distinct pressure conditions, allowing for the comparison of their performance across different mechanical environments.

2.3 | Setup Cycle Support

As mentioned above, electrochemical cycling was carried out under three different mechanical pressure configurations, which were applied to pouch cells taken from the same batch. In all cases, the cells were cycled in the same orientation, with the electrode sheets positioned horizontally relative to the ground. The first was an "unconstrained" mode, in which the cell was cycled freestanding without any support structure (top plate) and no pressure applied (NP cell). The two "constrained" modes were varied by the applied pressure levels: a low-pressure configuration (LP cell) and a high-pressure configuration (HP cell). To apply the mechanical load on the cells, a dedicated support structure was utilized, consisting of two polished aluminum plates (each $10 \times 520 \times 150$ mm in dimension and 2.09 kg in weight) and a silicone thermal interface pad (RS Pro, thickness of 1.5 mm, thermal conductivity of 8.0 W/mK) attached between the pouch cell and each aluminum plate (Figure 1b). The silicone pads maintained electrical insulation, efficient thermal conductivity, and a uniform pressure distribution on the cell surface. Different methods for maintaining low- and high-pressure configurations were explored (Figure S1). In the low-pressure configuration, the pouch cell was placed between two aluminum plates with thermal interface pads, without any applied external lateral pressure. The only applied load resulted from the top plate's own weight (approximately 0.0004 MPa). For the high-pressure configuration, a clamping fixture was developed to actively apply uniform lateral mechanical pressure and replicate realistic battery pack conditions to the pouch cell. In this setup (Figure 1b), a spring-based clamping approach is implemented, commonly described in literature to simulate pack-level constraints [47, 48] and to ensure optimal cycling conditions [49, 50]. The aluminum plates, positioned on either side of the cell, were compressed by eight evenly distributed coil springs (Compression Spring VD-339V-01) with a spring rate of 94.155 N/mm and an initial length of 90 mm. The springs were radially supported by a shell-type spring carrier (Figure 1b). This configuration provided a uniform mean contact pressure of ~1.2 bar (0.116 MPa) to the cell surface, with each spring applying a force of 734.4 N (detailed calculation in the Supporting Information). This pressure is in addition to the load from the top plate's weight (approximately 0.0004 MPa). The pressure range is consistent with similar cell-level clamping setups (0.09–0.17 MPa [47–50]) and was set toward the lower end to prevent overconstraining the pouch cell, while maintaining realistic pack conditions. Minor pressure variations for the HP cell were introduced by changes in cell thickness with the cells' SOC [51, 52]. Such a change affected the clamping pressure, which increased to 0.122 MPa at SOC 100%, reflecting the mechanical expansion of the cell thickness.

Furthermore, each fixture configuration was equipped with a PT100 temperature sensor attached to the surface of the pouch cell to monitor the cell's surface temperature during cycling. For the low- and high-pressure setups, a small edge was milled in the base plate to embed/host the temperature sensor, while avoiding any damage to the pouch cell and preserving the uniformity of applied pressure.

2.4 | PXRD

High-energy PXRD radiography measurements were conducted at room temperature at the P02.1 beamline (Figure S2) of the PETRA III synchrotron, DESY (Hamburg, Germany). The experiments were performed in Debye–Scherrer geometry using a monochromatic X-ray beam with a beam size of $1 \times 1\ mm^2$. The measurements were carried out over the course of several experimental campaigns, adopting a similar measurement strategy with minor variations between individual experiments. The X-ray wavelength was $\lambda \sim 0.207$ Å (corresponding to 60 keV photon energy), while exposure times were fixed to either 5 or 10 s per diffraction pattern [53].

The beamline was operated in a high-resolution configuration, with a sample-to-detector distance (SDD) ranging between 1.74 and 2.14 m. Two different area detectors were used during the experiments: either a Pilatus 3X CdTe 2 M detector (Dectris) with a pixel matrix of 1475×1679 pixels and a pixel size of $172 \times 172\ \mu m^2$ or a 2D Varex XRD 4343CT detector featuring 2880×2880 pixels with $150 \times 150\ \mu m^2$ pixel size. The detailed instrumental parameters for each experiment are listed in Table S1. The instrument calibration was performed prior to the measurements using a LaB_6 SRM 660c standard reference material. Data reduction was carried out by azimuthal integration using the pyFAI library [54, 55].

The cells were mounted on a setup allowing 2D translation of the large cell surface perpendicular to the synchrotron beam. To ensure cell stability, each pouch cell was mounted between two 10-mm-thick PMMA plates fastened together using eight screws to increase mechanical stability and prevent damage to the cell (Figure S2). The assembled cell support was attached to an aluminum profile, further fixed to motorized translation stages. The experimental setup ensured a stable, reproducible and vibration-free scanning during the entire radiography sequence. The PXRD radiography measurements were carried out using varying step sizes in both directions across the full cell area (Figure S2). The detailed step size and scanning grids used are listed in Table S1.

All PXRD radiography measurements were conducted on cells at 100% SOC. After transportation, the pouch cells were connected to a BioLogic VMP-300 potentiostat to recharge them prior to measurement and prepare them for storage after the experiment. Charging was performed using a CC–CV protocol at a C/3 current rate, with a voltage limit of 4.2 V and a cutoff current of C/20. Following the radiography experiments, the cells were discharged using a constant current of 1/3 C until reaching 3 V. In total, four PXRD radiography measurements were carried out at SOC = 100% on three different pouch cells. The unconstrained cell was measured in both fresh and aged states, while the two constrained cells (low and high pressure) were measured only in the aged state. The relatively large dimensions and weight of the pouch cells introduced challenges during installation and alignment of them at the beamline. Even with precise positioning using a dial gauge, slight tilts of the mounted cells relative to the incident beam introduced small variations in the SDD, which were traceable through the systematic shift of XRD peaks. An initial SDD was determined with a standard LaB_6 (SRM660c) reference sample placed at the cell center, which was further used for azimuthal integration of the collected diffraction patterns. Minor systematic shifts in peak positions were observed across the dataset, which were attributed to small changes in the effective SDD during the measurements. To correct for the minor systematic shifts in peak positions, the 111 Cu reflection was used as an internal standard. Peak position was determined by using the fit of the 111 Cu reflection to a pseudo-Voigt function. The deviation of the SDD was calculated from the reference and local positions of Cu reflection in transmission geometry (Equations E5 and E6 in the Supporting Information) [17]. With the corresponding deviation from the initial SDD, the angles in each diffraction pattern were corrected individually, thus ensuring that the diffraction angles accurately reflect the sample geometry despite minor misalignments. Following this correction, selected lithiated graphite reflections (001 LiC_6, 002 LiC_{12}, 006 LiC_{30}, 008 LiC_{40}, and 002 graphite) as well as two cathode reflections (003, 113) were fitted with pseudo-Voigt functions. The relative lithiation of the anode was calculated primarily from the peak areas.

3 | Results and Discussion

The implementation of different pressure regimes on large pouch cells (Figure 1) clearly and unambiguously revealed an influence on their performance and lifetime, directly traceable in the recorded electrochemical data. As mentioned, cell cycling was carried out using a protocol that combined a batch of 200 relatively fast cycles with RPC checks in between. Distinctly different cycling behaviors were observed for each cell, affecting the reached DOD, capacity, cycle number, temperatures of the cell during cycling, the corresponding internal resistances, and the lithiation homogeneity of the electrodes.

3.1 | Cycle Aging Under Mechanical Pressure

Focusing solely on the voltage vs. capacity plots (Figure S3) obtained during the RPCs gives the impression that the three different studied cells exhibit similar degradation. Systematic shifts of the voltage curves toward lower capacities, accompanied by corresponding increased/decreased charge/discharge voltages, display that the major capacity utilization of the large pouch cells occurs in a voltage window of 3.4–4.2 V. Analyses of incremental capacity and differential voltage confirm the degradation in each aged cell (Figure S4) with peak intensities decreased, shifted, and progressively broadened, indicating structural and kinetic degradation and decreasing homogeneous lithium distribution [56, 57]. Neither additional shoulders in the DVA nor a shift of graphite lithiation peaks toward higher capacities were observed, indicating no silicon in the anode [58], which is in agreement with Ref. [24].

However, despite a relatively similar degradation behavior on the qualitative level, the rate of capacity fade has been found to be different among the studied cells. Analyzing results from RPC cycles revealed the fastest degradation for the unconstrained NP cell, followed by the HP cell.

Slowest capacity fade and highest discharge energy throughput ($E = \int V(t)I(t)dt$) was observed for the LP cell (Figure 2a) over the whole cycle life, with a similar reduction in SOH as the HP cell up to ~200 kWh of discharge energy throughput. Afterward, the performance diverges: The HP cell shows accelerated capacity fade, whereas the LP cell shows a slower and more stable degradation rate. However, focusing on the cycle of the cells showed that the NP cell reached the cutoff SOH of 80% after 1000 cycles (Figure S5) with a total discharge energy throughput of 127 kWh (charge energy throughput: 152 kWh). Contrary, both "constrained" cells achieved significantly extended cycle life, exceeding 8000 cycles. While the HP cell showed a higher cycle number and lower total discharge energy throughput of 663 kWh (charge energy throughput: 793 kWh), the LP cell reached reduced cycle number but higher discharge energy throughput of 856 kWh (charge energy throughput: 1019 kWh). In contrast to relatively "mild" reference cycles, the "fast" cycling revealed the performance of the cells and their degradation, different from the observed trends during the RPC (Figure 2b). The achieved capacity of each cell is drastically reduced (relative to the achieved capacity during the RPC), resulting in significantly lower DOD values and influencing their total cycle number. For the NP cell, the DOD is observed dropping to < 60% and for the constrained cells to < 50%. This reduction is directly linked to the specific cycle parameters of real cycling, which involve increased charging or discharging currents and variations in the applied external pressure. However, all three cells display a similar three-stage evolution of accessible DOD throughout cycling, characterized by an initial reduction, a subsequent partial recovery, and a final linear

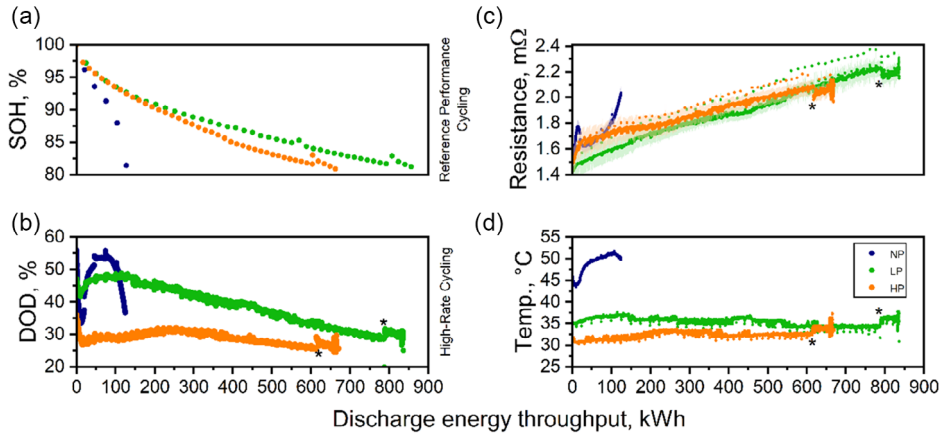

FIGURE 2 | Electrochemical performance of pouch cells cycled at different pressure conditions (NP, LP, and HP) showing (a) SOH capacity fade (relative discharge capacity at C/10) during the RPC and (b) DOD capacity fade (relative discharge capacity at 2C) during high-rate cycling, together with the evolution of (c) internal resistance and (d) corresponding maximum cycle temperature during high-rate cycling as a function of discharge energy throughput. Asterisks mark the position of restart of cell cycling after 8 days due to an unplanned software update.

decrease of the DOD toward the EOL. While this sequence is qualitatively consistent across the cells, the extent and timing of the processes differ substantially. The NP cell exhibited the most pronounced initial fade and recovery, reaching the highest accessible DOD under real cycling conditions.

On the contrary, the LP and HP cells show lower achieved DOD with smoother fade and a shifted recovery. Consequently, the reduced accessible DOD at high-rates and under varying pressure directly limits the storable (charge) and deliverable (discharge) energy per cycle (Figure S6), with lower discharge energies per cycle, reducing their round-trip energy efficiency ($\eta = \frac{E_{\text{discharge}}}{E_{\text{charge}}}$). However, the observed variation in the DOD during cycling can be directly translated to the achieved cumulative discharge energy throughput and cycle number. Furthermore, a reduction in the DOD for each cell was observed for the first cycles after each RPC.

Thus, the absence of external pressure can increase the energy throughput per cycle but results in rapid degradation and a reduced lifetime. In contrast, applying external pressure significantly extends the cycle life of the studied cells and enhances cumulative energy throughput, with low pressure (LP cell) providing a compromise between accessible DOD, stability, and long-term performance.

The observed behavior of cell capacity can be attributed to the change in internal resistance of the different cells during electrochemical cycling. Internal resistance was evaluated using two complementary approaches: DCIR measurements (1C, 20 s) during the RPCs (Figure S7) and apparent DC resistance extracted from the initial voltage drop (2C, 10 s) under high-rate cycling conditions (Figure 2c). In both cases, the resistance R_{DC} was calculated based on Ohm's law ($R_{\text{DC}} = \Delta V / \Delta I$). Extracted RPC resistances have been found to be dependent on the SOC of the cell, with R (SOC 10%) displaying the highest aging-driven growth.

Note, a certain drop of internal resistance is observed at higher cycle numbers, which is attributed to the restart of cell cycling after 8 days due to an unplanned software update in the test field. With such a rest phase, the load on the cells, introduced by high currents and evolving temperature, was reduced, resulting in the relaxation of the cells, which can reduce the internal resistance. After the continuation of cycling, the probed internal resistances returned to their initial values and then exceeded them. Among the configurations, the HP cell initially exhibited the highest internal resistance at the beginning-of-life (BOL), while at the EOL, the LP cell showed the highest resistance values (Figure S8). In general, the NP cell showed the most substantial increase in resistance until reaching the EOL, while the constrained cells exhibited slower, more gradual growth, with the LP cell showing a slightly steeper slope compared to the HP cell (Figure S9). The resistance evolution under high-rate cycling conditions followed a similar trend (Figure 2c). The NP cell showed a substantial increase in resistance in the initial state followed by a partial recovery and subsequent continuous rise, aligning its characteristic capacity fade (Figure 2b) and temperature evolution (Figure 2d). Contrary, the constrained cells exhibited a more gradual evolution, though the HP cell experienced higher resistance than the LP during the first cycles. Consequently, temperature of constrained cells was reduced due to additional passive cooling from the pressure setup, decoupling internal resistance evolution from temperature evolution. Further significant short-term effects were observed following each RPC. The first two fast-charging cycles showed a temporary increased resistance, which then recovered. This effect was matched by a reduced DOD and temperature visible at the onset of fast cycling (Figure 2b). After recovery and continuous cycling, the resistance slightly increased again until reaching the next RPC. This behavior was found to be similar for all fast-charging cycles, except for the first 200 cycles of the NP cell. These observations indicate that applying mechanical pressure increases the internal resistance at BOL and reduces the rate of internal resistance growth during cycling. However, this reduced resistance growth does not directly translate into higher energy throughput. Instead, the benefits of pressure in mitigating resistance growth are counterbalanced by limitations in accessible DOD and output energy. Thus, the application of pressure represents a trade-off between minimizing resistance increase, maintaining energy accessibility, and extending cycle life. During the RPC, no significant temperature differences were observed between the cells (Figure S10). The test field temperature was controlled at 25°C ± 1°C, and the maximum cell temperature recorded during the RPC was 27°C. Such minor variations can be attributed to

seasonal fluctuations in the ambient environment rather than cell-specific effects. Contrary, under real cycling conditions, significant temperature dynamics were observed. Thus, each cycle showed a dedicated temperature profile, similar for each cell. During each discharge cycle using 2C current, the temperature increased (Figure S11). Immediately after discharge, charging was initiated, exhibiting a complex temperature evolution. First, a short period of continued temperature increase, immediately after the discharge, was observed, reflecting thermal inertia. Afterward, a slow temperature decrease was observed during the applied CC phase (1C current), followed by accelerated cooling during the CV phase. Cooling was stopped right after the discharge of the next cycle started, repeating the temperature cycle and representing the dynamic balance between heat generation and dissipation during cycling. The magnitude of the temperature rise depended strongly on the applied passive cooling pressure environment (Figure 2d). Thus, the unconstrained cell showed the highest maximum temperatures, exceeding 50°C, which is known to contribute to a faster capacity fade, affecting in particular anode stability, as already discussed in Ref. [59]. In comparison, the constrained cells showed comparable lower maximum temperatures during the real cycling, with the LP cell exceeding temperatures of the HP cell (on average 3°C). Note, the temperature fluctuations observed for the constrained cells at high cycle count are the result of resetting the conditioning system in the test field. At first glance, this appears counterintuitive, as the voltage–capacity behavior during the initial real cycling indicates increased polarization and reduced accessible DOD in the HP cell (Figure S12), and initial DCIR measurements revealed higher internal resistance for the HP cell at low cycle numbers. However, thermal behavior is not solely dictated by electrochemical overpotentials, but also by the cell's ability to dissipate heat. Thus, the silicone pads and the aluminum plates surrounding the constrained cells act as passive cooling elements, and the higher pressure ensures improved contact between the electrode stack and the plates. This enhances thermal conductivity, allowing for more efficient heat dissipation [60].

Furthermore, the temperature evolution was closely linked to the achieved DOD and internal resistance of the cells. For the NP cell, temperature and capacity evolved in parallel, with a decrease in cell temperature corresponding to an increase in internal resistance (Figure 2b–d). This effect was only weakly visible in the constrained cells due to additional passive cooling (Figure S13). Furthermore, after RPCs, the observed reduced DOD, increased round-trip efficiency, and internal resistance at the initial cycles of the fast cycling correlated with the temperature evolution on the cell surface. Thus, the cell temperature during the RPC is close to the defined 25°C within the test field (Figure S10). Upon fast charging, it took the cells up to two cycles to reach their typical operating temperature (Figure S14) and the corresponding higher DOD. This behavior was more pronounced in constrained cells, due to increased cooling efficiency. However, the thermal conditions of a cell can strongly influence ionic conductivity and charge-transfer kinetics, particularly in mechanically stabilized cells with higher thermal inertia [61].

As a result, although the HP cell may experience greater overpotentials due to electrode compression, it benefits thermally from enhanced passive cooling and reduced surface heating. In contrast, the NP cell, lacking mechanical stabilization, suffers from poor heat transfer, leading to elevated surface temperatures and in turn increased DOD during high-current operation.

3.2 | Lithiation Inhomogeneity

In literature, it is commonly accepted that cell aging stabilizes a heterogeneous state. The electrochemical aging of the studied pouch cells under varying external pressure conditions induces the formation of lithiation inhomogeneity across both the graphite anode and the NMC cathode, which can be directly identified in the collected PXRD radiography patterns (Figure S15). Such inhomogeneity evolves with SOH and is strongly dependent on the applied mechanical conditions. In the fresh reference cell, the graphite reflections are dominated by the LiC_6 phase, accompanied by weaker contributions from the LiC_{12} phase, consistent with a nearly complete lithiation of the graphite at 100% SOC. Aging typically results in the loss of lithium inventory, leading to a reduction in the lithiation degree at the anode, reflected in a decrease in the amount of Stage I, accompanied by an increase in the fraction of Stage II concentration due to the presence of weaker lithiated graphite with $LiC_{x>12}$. Correlated behavior is also observed in the cathode phase, reflected in the shift of the NMC 003 reflection, representing altered delithiation behavior with cycling [62].

At first glance, a similar degradation occurs in all NP, LP, and HP cells. However, both qualitative and quantitative analyses revealed distinct deviations in the diffraction signatures of the anode lithiation between different protocols. At the full-cell level, the fresh cell shows a relatively homogeneous lithiation in the anode, with an average lithium concentration of $\langle x \rangle = 0.90 \pm 0.07$ in Li_xC_6 (Figure 3). Some minor deviations are detectable (e.g., slightly lower lithiation takes place close to the positive current tab, and a maximum of lithiation occurs closer to the cell center). The extended electrochemical aging of the cells to 80% SOH introduces a loss of movable lithium and an increase in lithium heterogeneity across the electrodes.

In the NP configuration, the average lithium concentration decreases by 15% to $\langle x \rangle = 0.77 \pm 0.08$, exhibiting pronounced deviations from an even constant distribution. Thus, regions of low lithium concentration are observed at both current tabs, while the lithiation grade of the anode is increased at the center of the cell. Nevertheless, an additional spot of low lithium concentration was observed at ~225 mm cell height. The introduction of a low external load (LP) significantly mitigates this effect, leading to a more uniform lithium distribution with an average concentration of $\langle x \rangle = 0.81 \pm 0.08$. Nonetheless, small regions of low-lithium concentrations are still present near the positive tab (top), in the center of the cell, and toward the negative current tab (bottom). However, directly at the negative current tab, the lithium concentration is relatively high compared to the NP cell. Overall, the introduction of low pressure can seemingly at least partially reduce the formation of lithium inhomogeneity by suppressing loose contact of the electrode sheets and corresponding local overpotentials. On the contrary, the HP condition produces a distinct lithium redistribution pattern. While the average lithiation reaches $\langle x \rangle = 0.78 \pm 0.15$, a pronounced gradient develops across the whole cell, showing a ring-like lithiation profile. Potentially, there are weak hints of such a profile visible in the anode lithiation of the LP cell.

However, in the HP cell, the lithium concentration of the anode in the central region falls to $x \approx 0.6$, while the cell edges remain at high lithium concentrations ($x \approx 0.9$). In addition, within the observed ring, anisotropy was present, showing higher lithium

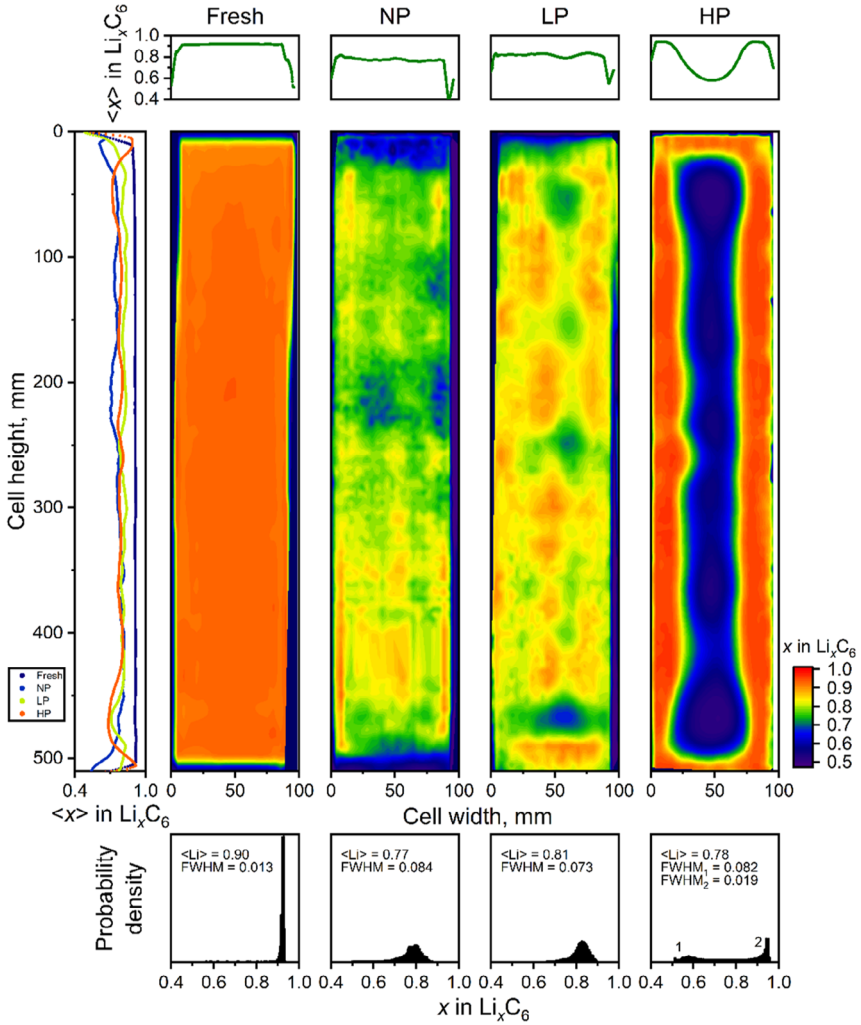

FIGURE 3 | Results of PXRD radiography measurements show calculated lithium concentration variations in the anode across the pouch cell area from positive (top) to negative (bottom) terminal for the fresh cell, the NP cell, the LP cell, and the HP cell. The corresponding average lithium concentration profiles along the cell height (left) and the width (top) are also displayed. The histograms at the bottom illustrate the distribution of lithium concentrations, quantified by the average concentration and the full width at half maximum (FWHM) obtained from Gaussian fits.

concentration along the long edges compared to the lithium concentration along the short edges. The calculated average line profiles across the cell width further confirm that the lithium concentrations at the edges are close to the fresh reference values (Figure 3).

Overall, these results demonstrate that external pressure and passive cooling can have a strong influence on the spatial distribution of lithium concentrations in both the anode and the cathode (Figures S16 and S17). Low pressure slightly reduces lithium inhomogeneity compared to the unconstrained state, while high pressure promotes systematic anisotropic lithium redistribution, leading to a ring-like profile in both anode and cathode.

3.3 | Coupling of Structural Properties and Electrochemical Behavior Under Pressure

The observed differences in electrochemical cycling and inhomogeneity in the diffraction data under varying pressure conditions highlight the complex interplay between external mechanical constraints and cell performance. External pressure defines the mechanical load on the electrode stack, thereby influencing electrochemistry, internal resistance, temperature evolution, and the spatial redistribution and exchange of lithium within and between the electrodes. According to Ref. [63], external pressure can suppress stack swelling, which mitigates delamination and lithium plating in mechanically constrained configurations. Furthermore, prior studies [33, 35, 36, 64, 65] demonstrated that compression enhances interparticle contact, reduces contact resistance, and stabilizes internal resistance growth. This trend is consistent with the observed internal resistances, showing that constrained cells exhibited a slower increase in resistance compared to the unconstrained NP cell, confirming a stabilizing effect during long-term cycling. However, at the BOL, the HP cell showed the highest internal resistance values at every probed SOC state, which likely stem from the decrease of porosity, increase in tortuosity and resulting restrictions in the ion transport during the cycling within the pouch cell [56, 66]. Thus, concentration polarization dominated with increasing pressure. Furthermore, this effect explains the increased polarization of the HP cell in the voltage–capacity curves (Figure S12) and the corresponding reduction in the accessible DOD compared

to the LP and NP configuration. By contrast, reducing the applied pressure decreased overpotentials, resulting in lower charge voltages and higher discharge voltages. In addition, the lack of pressure and influence of the aluminum plates acting as heat sinks in the NP configuration led to an increased DOD, but at the expense of faster capacity fade resulting from additional enhanced thermal aging.

Such an effect also influences the distribution of lithium concentrations within the electrodes, observed in the collected structural PXRD radiography data. At HP conditions, the lithium concentration in the electrode center decreased, while it remained like the BOL values at the edges (Figure S8), forming a ring-like lithiation profile. While this spatial lithiation heterogeneity represents a direct experimental observation obtained from synchrotron PXRD radiography, the underlying mechanisms responsible for this distribution, however, cannot be measured directly in the present study and are therefore interpreted based on experimental trends and literature evidence. Thus, we propose that this gradient arises from a complex mechanism that represents an interplay of electrochemistry, structure, and mechanical properties. On the one hand, external pressure significantly reduces the porosity of the electrodes and separator, thereby increasing tortuosity and decreasing the effective amount of electrolyte required to completely fill the pore structure [66]. On the other hand, electrochemical cycling results in particle expansion during charging, which can further reduce the pore volume [23, 51, 52]. These coupled effects are expected to influence electrolyte distribution within the cell. Previous studies have reported pressure-induced electrolyte motion and redistribution, which can lead to localized variations in pore filling, transport limitations, and heterogeneous electrochemical activity [23, 56, 67]. Within this mechanistic framework, the observed lithiation gradient is consistent with a scenario in which electrolyte shifts toward the edges of the cell under compression and increasing SOC, while central regions experience reduced pore filling. Additionally, while commercial cells are usually designed to contain excess electrolyte [23, 68, 69], under high-pressure (HP) conditions, the reduced pore volume and the redistribution of the electrolyte can lead to insufficient electrolyte availability in certain areas. This may result in low pore fill ratios in the center of the cells, while the edges may have high pore fill ratios. Consequently, this imbalance can promote localized aging in the center of the cell [46]. Overextended cycling, the combination of pressure and electrolyte motion, reduces the availability of electrolyte in the central regions of the cell. This again leads to an increase in local overpotential, which, when combined with extensive cycling, results in electrode degradation. This degradation is reflected in a diminishing lithiation profile in the center of the cell (see Figure 3). External pressure has both benefits and drawbacks. On one hand, it helps suppress swelling, prevents delamination and plating, and stabilizes interfacial resistance. On the other hand, it reduces pore volume, increases tortuosity, and drives electrolyte motion, all of which limit mass transport and enhance concentration overpotentials. As a result, while moderate pressure improves the homogeneity of lithiation, maintains a higher average level of lithiation, and supports long-term stability, excessive pressure can lead to significant lithium gradients, depletion of the electrolyte in the central region, and transport limitations. These issues ultimately reduce the accessible depth of discharge and accelerate degradation [65]. Corroborating these findings, post mortem analysis confirmed that mechanical constraints directly influence interfacial degradation, as residues of the ceramic separator coating were found preferentially attached to locally degraded electrode regions, consistent with the observed inhomogeneous lithiation (Figures S19 and S20). Moreover, the detection of electrically isolated graphite particles and local lithium plating provides clear evidence that poor interfacial contact (NP) and elevated local overpotentials (HP) are key drivers of the observed structural inhomogeneity.

4 | Conclusion

The electrochemical aging of large-format pouch cells under different external pressure conditions was systematically investigated by combining long-term cycling experiments, reference performance testing, temperature monitoring, and synchrotron PXRD radiography measurements and postmortem analyses. The cells were cycled under practical high-current conditions (1C charge, 2C discharge) with and without external mechanical load, while RPC tests at low current provided insight into resistance evolution and capacity fade. Structural characterization was performed in a fresh state and at 80% SOH, enabling the direct correlation of electrochemical performance with lithiation homogeneity across the electrode stack. The electrochemical data revealed that external pressure has a strong influence on cycling stability, resistance evolution, and accessible DOD. While the unconstrained cell showed the highest initial DOD, it suffered from rapid capacity fade, fast resistance growth, elevated operating temperatures, and ultimately the shortest lifetime. Constrained cells, in contrast, exhibited reduced accessible DOD but significantly improved cycle life and lower operating temperatures. Internal resistance analysis revealed that external pressure stabilizes contact resistance and slows resistance growth. However, concentration polarization dominated at high current densities, particularly in high-pressure cells. Temperature monitoring further confirmed that constrained configurations benefited from improved heat dissipation through mechanical contact with silicone sheets and aluminum compression plates, reducing thermal stress compared to unconstrained cycling. PXRD radiography provided spatially resolved insight into the pressure-dependent distribution of lithiation in the electrodes. While fresh cells displayed homogeneous lithiation, aging induced significant inhomogeneities. Under HP conditions, a pronounced ring-like lithium concentration profile developed, with central depletion and edge enrichment, whereas moderate pressure partially suppressed such gradients. These effects were attributed to a combination of reduced electrode porosity, increased tortuosity, and pressure-induced electrolyte motion, resulting from the applied pressure and repeated particle expansion and contraction during electrochemical cycling. This process promotes outward electrolyte motion, gradually depletes central regions, and thereby increases local resistance and overpotentials.

In summary, this study enabled a direct link between external mechanical pressure, electrochemical degradation, and spatial lithiation heterogeneities. While pressure enhances cycling stability by suppressing electrode swelling, delamination, and thermal buildup, HP conditions induce substantial ionic transport limitations and electrolyte motion, which promote inhomogeneous lithiation and reduced accessible DOD. Moderate pressure thus emerges as optimal operating condition, balancing improved structural stability and lithium homogeneity with sustained long-term

performance. Further research should focus on whether a "sweet spot" in performance exists that links both extremes of high and low pressure applied. Moreover, it should investigate the evolution of lithium-ion cell performance under well-defined thermal conditions across varying pressure levels to decouple mechanical and thermal effects on aging behavior.

Author Contributions

Tobias Hölderle: conceptualization (equal), data curation (lead), formal analysis (lead), investigation (lead), methodology (equal), software (lead), validation (lead), visualization (lead), writing – original draft (lead). **Anna Smith**: methodology (equal), resources (equal), writing – review & editing (equal). **Nils Schmidgruber**: data curation (supporting), investigation (supporting), resources (supporting), validation (supporting), writing – review and editing (supporting). **Volodymyr Baran**: conceptualization (equal), data curation (equal), formal analysis (equal), investigation (equal), methodology (equal), resources (equal), validation (equal), writing – review and editing (equal). **Alexander Schökel**: data curation (equal), formal analysis (equal), resources (equal), software (supporting). **Lea Westphal**: data curation (equal), investigation (equal), methodology (supporting), validation (equal), visualization (supporting). **Vladislav Kochetov**: conceptualization (supporting), data curation (equal), formal analysis (equal), investigation (equal), methodology (supporting), software (equal), validation (equal), visualization (supporting). **Steffen Jokisch**: data curation (equal), formal analysis (supporting), investigation (supporting), methodology (supporting), resources (equal), validation (supporting), writing – review and editing (supporting). **Peter Müller-Buschbaum**: funding acquisition (lead), project administration (lead), resources (lead), supervision (lead), writing – review and editing (equal). **Anatoliy Senyshyn**: conceptualization (lead), data curation (equal), funding acquisition (equal), methodology (lead), project administration (lead), resources (equal), supervision (lead), validation (lead), writing – review and editing (lead).

Acknowledgments

The authors gratefully acknowledge the financial support provided by the Heinz Maier-Leibnitz Zentrum (Technische Universität München), German Federal Ministry of Education and Research (BMBF project 05K19VK3). We acknowledge DESY (Hamburg, Germany), a member of the Helmholtz Association HGF, for the provision of experimental facilities. Parts of this research were carried out at PETRA III. Data was collected using beamline P02.1 operated by DESY Photon Science. Beamtime was allocated for proposal I-20230255. The authors thank Josef Pfanzelt for the help with setting up the construction used at P02.1. The cell testing and disassembly was done at KIT Battery Technology Center (KIT-BATEC) and contributes to the research performed at the Center for Electrochemical Energy Storage Ulm & Karlsruhe (CELEST).

Open Access funding enabled and organized by Projekt DEAL.

Conflicts of Interest

The authors declare no conflicts of interest.

Data Availability Statement

The data that support the findings of this study are available from the corresponding author upon reasonable request.

References

1. A. Yoshino, "The Birth of the Lithium-Ion Battery," *Angewandte Chemie International Edition* 51 (2012): 5798–5800.

2. O. Gröger, H. A. Gasteiger, and J.-P. Suchsland, "Review—Electromobility: Batteries or Fuel Cells?," *Journal of the Electrochemical Society* 162 (2015): A2605.

3. D. Andre, S.-J. Kim, P. Lamp, et al., "Future Generations of Cathode Materials: an Automotive Industry Perspective," *Journal of Materials Chemistry A* 3 (2015): 6709–6732.

4. M. Winter and R. J. Brodd, "What Are Batteries, Fuel Cells, and Supercapacitors?," *Chemical Reviews* 104 (2004): 4245–4270.

5. Y. Yerkinbekova, A. Kumarov, B. Tatykayev, A. Mentbayeva, E. Repo, and E. Laakso, "Ni-Rich Cathode Materials with Concentration Gradients for High-Energy and Safe Lithium-Ion Batteries: A Comprehensive Review," *Journal of Power Sources* 626 (2025): 235686.

6. A. Smith, P. Stüble, L. Leuthner, A. Hofmann, F. Jeschull, and L. Mereacre, "Potential and Limitations of Research Battery Cell Types for Electrochemical Data Acquisition," *Batteries & Supercaps* 6 (2023): e202300080.

7. T. Marks, S. Trussler, A. J. Smith, D. Xiong, and J. R. Dahn, "A Guide to Li-Ion Coin-Cell Electrode Making for Academic Researchers," *Journal of the Electrochemical Society* 158 (2011): A51.

8. V. Murray, D. S. Hall, and J. R. Dahn, "A Guide to Full Coin Cell Making for Academic Researchers," *Journal of the Electrochemical Society* 166 (2019): A329.

9. L. Reuter, L. J. Reinschlüssel, and H. A. Gasteiger, "3-Electrode Setup for the Operando Detection of Side Reactions in Li-Ion Batteries: The Quantification of Released Lattice Oxygen and Transition Metal Ions from NCA," *Journal of the Electrochemical Society* 171 (2024): 100524.

10. D. Pritzl, J. Landesfeind, S. Solchenbach, and H. A. Gasteiger, "An Analysis Protocol for Three-Electrode Li-Ion Battery Impedance Spectra: Part II. Analysis of a Graphite Anode Cycled vs. LNMO," *Journal of the Electrochemical Society* 165 (2018): A2145.

11. M. D. L. Garayt, M. B. Johnson, L. Laidlaw, et al., "A Guide to Making Highly Reproducible Li-Ion Single-Layer Pouch Cells for Academic Researchers," *Journal of the Electrochemical Society* 170 (2023): 080516.

12. N. Ogihara, S. Kawauchi, C. Okuda, Y. Itou, Y. Takeuchi, and Y. Ukyo, "Theoretical and Experimental Analysis of Porous Electrodes for Lithium-Ion Batteries by Electrochemical Impedance Spectroscopy Using a Symmetric Cell," *Journal of the Electrochemical Society* 159 (2012): A1034.

13. P. Wang, R. Xiong, W. Shen, and F. Sun, "Aging-Induced, Rate-Independent Lithium Plating: A Complete Mechanism Analysis Throughout the Battery Lifecycle," *Applied Energy* 393 (2025): 126094.

14. Z. Guo, Z. Ma, W. Zhao, S. Wang, H. Zhao, and L. Ren, "Quantitative Investigation on the Overcharge Cycling-Induced Severe Degradation of Electrochemical and Mechanical Properties of Lithium-Ion Battery Cells," *Energy* 318 (2025): 134900.

15. B. Liu, Y. Jia, C. Yuan, et al., "Safety Issues and Mechanisms of Lithium-Ion Battery Cell upon Mechanical Abusive Loading: A Review," *Energy Storage Materials* 24 (2020): 85–112.

16. S.-M. Bak, Z. Shadike, R. Lin, X. Yu, and X.-Q. Yang, "In Situ/Operando Synchrotron-Based X-Ray Techniques for Lithium-Ion Battery Research," *NPG Asia Materials* 10 (2018): 563–580.

17. D. R. Sørensen, R. Gordon, A. Smith, I. Kantor, and M. R. V. Jørgensen, "In Operando Evaluation of Heterogeneity Development in Fast-Cycled Single-Layer Pouch Cells," *Chemistry of Materials* 36 (2024): 10871–10885.

18. A. Senyshyn, H. Ehrenberg, J. Reedijk, and K. R. Poeppelmeier, *Comprehensive Inorganic Chemistry III*, ed. J. Reedijk, and K. R. Poeppelmeier, (Elsevier, 2023): 329–367, Third Edition.

19. A. Senyshyn, M. J. Mühlbauer, K. Nikolowski, T. Pirling, and H. Ehrenberg, ""In-Operando" Neutron Scattering Studies on Li-Ion Batteries," *Journal of Power Sources* 203 (2012): 126–129.

20. L. Westphal, V. Kochetov, V. Baran, et al., "Temperature-Resolved Crystal Structure of Ethylene Carbonate," *Journal of Physical Chemistry C* 129 (2025): 11546–11553.

21. T. Hölderle, V. Baran, A. Schökel, et al., "Understanding the Temperature–Induced Decomposition of Commercial Nickel–Cobalt–Aluminum Oxide ($LiNi_{0.8}Co_{0.15}Al_{0.05}O_2$) Electrodes," *Batteries & Supercaps* 8 (2025): 2500421.

22. S. Stock, J. Hagemeister, S. Grabmann, et al., "Cell Teardown and Characterization of an Automotive Prismatic LFP Battery," *Electrochimica Acta* 471 (2023): 143341.

23. S. Solchenbach, C. Tacconis, A. Gomez Martin, et al., "Electrolyte Motion Induced Salt Inhomogeneity – a Novel Aging Mechanism in Large-Format Lithium-Ion Cells," *Energy & Environmental Science* 17 (2024): 7294–7317.

24. N. Wassiliadis, M. Steinsträter, M. Schreiber, et al., "Quantifying the State of the Art of Electric Powertrains in Battery Electric Vehicles: Range, Efficiency, and Lifetime from Component to System Level of the Volkswagen ID.3," *eTransportation* 12 (2022): 100167.

25. F. J. Günter and N. Wassiliadis, "State of the Art of Lithium-Ion Pouch Cells in Automotive Applications: Cell Teardown and Characterization," *Journal of the Electrochemical Society* 169 (2022): 030515.

26. S. Menner, J. Siehr, and M. Buchholz, "Investigation of Current Distributions of Large-Format Pouch Cells with Individual Temperature Gradients by Segmentation," *Journal of Energy Storage* 35 (2021): 102300.

27. P. J. Osswald, S. V. Erhard, A. Noel, et al., "Current Density Distribution in Cylindrical Li-Ion Cells during Impedance Measurements," *Journal of Power Sources* 314 (2016): 93–101.

28. D. Schreiner, T. Zünd, F. J. Günter, et al., "Comparative Evaluation of LMR-NCM and NCA Cathode Active Materials in Multilayer Lithium-Ion Pouch Cells: Part I. Production, Electrode Characterization, and Formation," *Journal of the Electrochemical Society* 168 (2021): 030507.

29. D. Petz, M. J. Mühlbauer, V. Baran, et al., "Lithium Distribution and Transfer in High-Power 18650-Type Li-Ion Cells at Multiple Length Scales," *Energy Storage Materials* 41 (2021): 546–553.

30. A. Singh, D. Sharma, and P. Kumari, "Integrated framework for thermo-mechanical crash finite element analysis of 4680 lithium-ion battery cell and its strength prediction using neural networks," *Engineering Computations* 42 (2025): 1–21.

31. C. Allgäuer, F. Grenz, K. Abo Gamra, and M. Lienkamp, "Thermal Management of 4680 Battery Cells: Cell Design and Cooling Concept," *Journal of Energy Storage* 131 (2025): 117318.

32. S. Link, C. Neef, T. Wicke, et al., 2022.

33. S. Friedrich, S. Stojcevic, P. Rapp, et al., "Effect of Mechanical Pressure on Lifetime, Expansion, and Porosity of Silicon-Dominant Anodes in Laboratory Lithium-Ion Cells," *Journal of the Electrochemical Society* 171 (2024): 050540.

34. S. Arisetty, N. Jimenez, and K. Raghunathan, "In Situ Thickness Measurements During Cycling of Li-Ion Pouch Cells with Silicon Negative Electrodes," *Journal of the Electrochemical Society* 169 (2022): 080515.

35. S. Friedrich, S. Helmer, L. Reuter, J. L. S. Dickmanns, A. Durdel, and A. Jossen, "Effect of Mechanical Pressure on Rate Capability, Lifetime, and Expansion in Multilayer Pouch Cells with Silicon-Dominant Anodes," *Journal of the Electrochemical Society* 171 (2024): 090503.

36. G. Berckmans, L. De Sutter, M. Marinaro, et al., "Analysis of the Effect of Applying External Mechanical Pressure on Next Generation Silicon Alloy Lithium-Ion Cells," *Electrochimica Acta* 306 (2019): 387–395.

37. H. Chen, Y. Xu, Y. Wu, Z. Wang, and Y. Huang, "External Pressure Effects on Thermal Runaway in Prismatic LiFePO4 Batteries: Mechanistic Insights for Safer Battery Systems in Electric Vehicles," *eTransportation* 26 (2025): 100488.

38. R. Li, D. Ren, S. Wang, et al., "Non-Destructive Local Degradation Detection in Large Format Lithium-Ion Battery Cells Using Reversible Strain Heterogeneity," *Journal of Energy Storage* 40 (2021): 102788.

39. A. Aufschläger, A. Durdel, L. Kraft, and A. Jossen, "Optimizing Mechanical Compression for Cycle Life and Irreversible Swelling of High Energy and High Power Lithium-Ion Pouch Cells," *Journal of Energy Storage* 76 (2024): 109883.

40. T. Schabenberger, S. Kücher, A. Aufschläger, and A. Jossen, "Impact of Applied and Preceding Pressure on Performance and Reversible Swelling of Lithium-Ion Pouch Cells with Varying Microporous Separators," *Journal of Energy Storage* 102 (2024): 113910.

41. W. Li, F. Yang, K. Wang, et al., "Clarifying the Effect of Pressure on Performance in Lithium-Ion Batteries," *Journal of the Electrochemical Society* 172 (2025): 010512.

42. M. Schreiber, K. Abo Gamra, P. Bilfinger, et al., "Understanding Lithium-Ion Battery Degradation in Vehicle Applications: Insights from Realistic and Accelerated Aging Tests Using Volkswagen ID.3 Pouch Cells," *Journal of Energy Storage* 112 (2025): 115357.

43. F. Pampel, S. Pischinger, and M. Teuber, "A Systematic Comparison of the Packing Density of Battery Cell-to-Pack Concepts at Different Degrees of Implementation," *Results in Engineering* 13 (2022): 100310.

44. Y. Preger, H. M. Barkholtz, A. Fresquez, et al., "Degradation of Commercial Lithium-Ion Cells as a Function of Chemistry and Cycling Conditions," *Journal of the Electrochemical Society* 167 (2020): 120532.

45. T. Baumhöfer, M. Brühl, S. Rothgang, and D. U. Sauer, "Production Caused Variation in Capacity Aging Trend and Correlation to initial Cell Performance," *Journal of Power Sources* 247 (2014): 332–338.

46. P. M. Attia, A. Bills, F. Brosa Planella, et al., "Review—"Knees" in Lithium-Ion Battery Aging Trajectories," *Journal of the Electrochemical Society* 169 (2022): 060517.

47. P. Höschele, S. F. Heindl, S. Erker, and C. Ellersdorfer, "Influence of Reversible Swelling and Preload Force on the Failure Behavior of a Lithium-Ion Pouch Cell Tested under Realistic Boundary Conditions," *Journal of Energy Storage* 65 (2023): 107228.

48. C. Essl, A. W. Golubkov, and A. Fuchs, "Comparing Different Thermal Runaway Triggers for Two Automotive Lithium-Ion Battery Cell Types," *Journal of the Electrochemical Society* 167 (2020): 130542.

49. M. Wünsch, J. Kaufman, and D. U. Sauer, "Investigation of the Influence of Different Bracing of Automotive Pouch Cells on Cyclic Liefetime and Impedance Spectra," *Journal of Energy Storage* 21 (2019): 149–155.

50. X. Zhang, J. Marco, G. Prentice, and D. Ainsworth, *2025 IEEE/AIAA Transportation Electrification Conference and Electric Aircraft Technologies Symposium (ITEC+EATS*, (2025): 1–6.

51. S. Schweidler, L. de Biasi, A. Schiele, P. Hartmann, T. Brezesinski, and J. Janek, "Volume Changes of Graphite Anodes Revisited: A Combined *Operando* X-Ray Diffraction and *In Situ* Pressure Analysis Study," *Journal of Physical Chemistry C* 122 (2018): 8829–8835.

52. X. Li, Z. Zhang, L. Gong, et al., "Modelling and Analysis of the Volume Change Behaviors of Li-Ion Batteries with Silicon-Graphene Composite Electrodes," *Chemical Engineering Journal* 470 (2023): 144188.

53. A.-C. Dippel, H.-P. Liermann, J. T. Delitz, et al., "Beamline P02.1 at PETRA III for High-Resolution and High-Energy Powder Diffraction," *Journal of Synchrotron Radiation* 22 (2015): 675–687.

54. G. Ashiotis, A. Deschildre, Z. Nawaz, et al., "The Fast Azimuthal Integration Python Library: *pyFAI*," *Journal of Applied Crystallography* 48 (2015): 510–519.

55. J. Kieffer, V. Valls, N. Blanc, and C. Hennig, "New Tools for Calibrating Diffraction Setups," *Journal of Synchrotron Radiation* 27 (2020): 558–566.

56. P. Morales Torricos, A. Gallenberger, D. Droese, J. Kowal, C. Endisch, and M. Lewerenz, "Analyzing the Impact of Electrolyte Motion Induced Salt Inhomogeneity Effect on Apparent Aging: Role of Current Rates and Temperature Effects in Accelerated Cyclic Aging Tests in Li-Ion Batteries," *Batteries & Supercaps* 9 (2026): e202500559.

57. P. Morales Torricos, C. Endisch, and M. Lewerenz, "Apparent Aging during Accelerated Cycling Aging Test of Cylindrical Silicon Containing Li-Ion Cells," *Batteries* 9 (2023): 230.

58. T. Hölderle, D. Petz, V. Kochetov, et al., "Structural Response of Silicon-Containing Graphite Anodes on Lithium Intercalation," *Energy Storage Materials* 75 (2025): 104042.

59. T. Hölderle, M. Monchak, V. Baran, et al., "Thermal Structural Behavior of ElectrochemicallyLithiated Graphite ($Li_x C_6$) Anodes in Li-ion Batteries," *Batteries & Supercaps* 7 (2024): e202300499.

60. A. Adeniran and S. Park, "Optimized Cooling and Thermal Analysis of Lithium-Ion Pouch Cell under Fast Charging Cycles for Electric Vehicles," *Journal of Energy Storage* 68 (2023): 107580.

61. J. Landesfeind and H. A. Gasteiger, "Temperature and Concentration Dependence of the Ionic Transport Properties of Lithium-Ion Battery Electrolytes," *Journal of the Electrochemical Society* 166 (2019): A3079.

62. T. Hölderle, M. Monchak, V. Baran, et al., "The Structural Behavior of Electrochemically Delithiated LixNi0.8Co0.15Al0.05O2 (x<1) Battery Cathodes," *Journal of Power Sources* 564 (2023): 232799.

63. A. Schommer, M. O. Corzo, P. Henshall, D. Morrey, and G. Collier, "Stack Pressure on Lithium-Ion Pouch Cells: A Comparative Study of Constant Pressure and Fixed Displacement Devices," *Journal of Power Sources* 629 (2025): 236019.

64. H. Nara, D. Mukoyama, R. Shimizu, T. Momma, and T. Osaka, "Systematic Analysis of Interfacial Resistance between the Cathode Layer and the Current Collector in Lithium-Ion Batteries by Electrochemical Impedance Spectroscopy," *Journal of Power Sources* 409 (2019): 139–147.

65. X. Du, Y. Hu, S.-Y. Choe, T. R. Garrick, and M. A. Fernandez, "Characterization and Analysis of the Effect of Pressure on the Performance of a Large Format NMC/C Lithium-Ion Battery," *Journal of Power Sources* 573 (2023): 233117.

66. P. Guan, L. Liu, and X. Lin, "Simulation and Experiment on Solid Electrolyte Interphase (SEI) Morphology Evolution and Lithium-Ion Diffusion," *Journal of the Electrochemical Society* 162 (2015): A1798.

67. T. Bond, S. Gasilov, R. Dressler, R. Petibon, S. Hy, and J. R. Dahn, "Operando 3D Imaging of Electrolyte Motion in Cylindrical Li-Ion Cells," *Journal of the Electrochemical Society* 172 (2025): 030512.

68. A. Bonakdarpour, I. Stoševski, A. Tiwari, S. R. Smith, B. M. Way, and D. P. Wilkinson, "Impact of Electrolyte Volume on the Cycling Performance and Impedance Growth of 18650 Li-Ion Cells," *Journal of the Electrochemical Society* 171 (2024): 020543.

69. F. J. Günter, C. Burgstaller, F. Konwitschny, and G. Reinhart, "Influence of the Electrolyte Quantity on Lithium-Ion Cells," *Journal of the Electrochemical Society* 166 (2019): A1709.

Supporting Information

Additional supporting information can be found online in the Supporting Information section. The authors have cited additional references within the Supporting Information.